



# Intensification of iron–boron complex association in silicon solar cells under acoustic wave action

Oleg Olikh<sup>1,\*</sup> , Vitaliy Kostylyov<sup>2</sup>, Victor Vlasuk<sup>2</sup>, Roman Korkishko<sup>2</sup>, and Roman Chupryna<sup>1</sup>

<sup>1</sup>Taras Shevchenko National University of Kyiv, 64/13, Volodymyrska Street, Kyiv 01601, Ukraine

<sup>2</sup>V. Lashkaryov Institute of Semiconductor Physic of NAS of Ukraine, 41, pr. Nauki, Kyiv 03028, Ukraine

Received: 8 February 2022

Accepted: 11 April 2022

© The Author(s), under exclusive licence to Springer Science+Business Media, LLC, part of Springer Nature 2022

## ABSTRACT

In this paper, we study the influence of ultrasound (US) on the recovery of light-induced degradation in Cz–Si solar cells. The complete recovery in the dark at near room temperature and the determined value of activation energy (0.656 eV) evidenced the iron–boron pair transformation-related degradation. The ability of extraction of FeB pair's parameters from short circuit current kinetics was discussed. It was revealed that the US loading leads to the acceleration of the FeB pair association. This effect was investigated for different US frequencies (0.3–30 MHz) and intensities (up to 1.3 W/cm<sup>2</sup>) as well as iron concentrations  $[(0.2–3) \times 10^{13} \text{ cm}^{-3}]$  in the solar cell over temperature range 300–340 K. It has been found that US longitudinal waves are more efficient than transverse waves. The experimentally observed phenomena are related to the decrease in iron migration energy (up to 10 meV) in the US stress fields.

## 1 Introduction

It is well known that ultrasound (US) can act efficiently on defect subsystems of semiconductor crystals and devices due to dissipation of US vibration energy, which is particularly intense in regions with periodicity disorder [1–3]. At US of subthreshold intensity, acoustically induced (AI) reconstruction of defects causes the reversible changes in charge concentration and mobility in crystals [4, 5], barrier height in Schottky structures [6, 7] as well as tunnel and recombination currents in p–n structures [3, 8]. Also, it seems promising to apply the US as an additional factor of influence during conventional

technological processes. In this case, semiconductor structures are usually found in nonequilibrium conditions, and the defect–impurity subsystem is capable of modifying easier under the action of elastic oscillations. For instance, the application of ultrasound loading (USL) during ion implantation facilitates the formation of ultra-shallow junctions [9], and intensifies the silicon surface layer amorphization [10]; USL applied during the production of porous silicon results in structural ordering [11] and when applied during ZnO deposition provides higher homogeneity of the films [12].

The silicon solar cells (SCs) constitute about 90% of the global photovoltaic production capacity. Iron is

Address correspondence to E-mail: olegolikh@knu.ua

one of the most relevant, omnipresent, and efficiency-limiting metallic impurities in p-type Si SCs [13, 14]. Therefore, the methods of defect engineering aimed at iron have practical importance. In silicon photovoltaics, one of the main methods of impurity deactivation and removing it from the operation zone is gettering Fe atoms at certain centers (extended defects, oxygen precipitates, or interfaces) [15]. A similar gettering can be realized during standard operations as phosphorus diffusion [16] or production of antireflection coating [17]. It is clear that the process efficiency depends on the mobility of iron atoms.

On the one hand, shallow acceptors (B, Al, Ga, In) are effective trapping sites for iron around room temperature and in darkness in p-Si due to electrostatic attraction between the negatively charged acceptors and the positively charged iron ions. All Fe-acceptor pairs are similar: complexes have two structural configurations with trigonal and orthorhombic symmetry and can be broken by intense illumination and/or annealing above 200 °C [13, 18]. On the other hand, the back surface field (BSF) cell and passivated emitter and rear cell (PERC) are the most popular designs that have been used in the mass-production of Si SCs, and both BSF and PERC are mainly based on boron-doped silicon wafers [19, 20]. Therefore the iron–boron pair is one of the most relevant complexes to the defect engineering in real SCs. This work aims to investigate experimentally how acoustic waves (AWs) influence the ability of iron to diffuse in silicon solar cells. The time of iron–boron pair association after light-induced dissociation was used as an indicator of iron ion mobility. The possibility of the ultrasound to change the state of FeB was shown previously [21, 22]. In particular, the FeB pair was revealed [22] to be dissociated in Cz–Si by the action of ultrasound with acoustic strain  $\xi_{\text{US}} = 10^{-5}$ – $10^{-4}$ . Furthermore, Ostapenko and Bell [22] regarded the resonance condition of pair dissociation and used 25–70 kHz. Besides, it was asserted [21] that in the case of predominant dissociated pairs, the ultrasound may promote the pairing reaction in contradistinction to the case of a high fraction of paired iron. But empirical evidence for this prediction is absent. In this work, (i) the wave frequency  $f_{\text{US}} = (0.3\text{--}30)$  MHz and subthreshold strain  $\xi_{\text{US}} < 2 \times 10^{-6}$  were used, which were deficient overcome the Coulombic

attraction between  $\text{Fe}_i$  and  $\text{B}_s^-$ ; (ii) the predominant dissociation of FeB was realized by intense illumination. Thus the association of FeB pair (the migration of  $\text{Fe}_i^+$ ) was firstly investigated in conditions of USL.

## 2 Experimental and calculation details

Experimental studies were performed on the samples of silicon SC ( $1.52 \times 1.535 \text{ cm}^2$ ) made based on single-crystal p-type silicon [100] wafers with the resistivity of about  $10 \text{ } \Omega \text{ cm}$  (boron doping level  $N_A = 1.4 \times 10^{15} \text{ cm}^{-3}$ ). The thickness of the wafers was  $380 \text{ } \mu\text{m}$ . Diffusion from the gas phase ( $\text{POCl}_3$ ) at  $940 \text{ } ^\circ\text{C}$  was performed on wafers resulting in an  $n^+$ -emitter layer on the front side (sheet resistance of about  $20\text{--}30 \text{ } \Omega/\square$ , thickness of  $0.7 \text{ } \mu\text{m}$ ). In addition, to reduce recombination losses and increase the conductivity of the contact layer, a  $p^+$  layer ( $10\text{--}20 \text{ } \Omega/\square$ ,  $0.6 \text{ } \mu\text{m}$ ) was formed by boron diffusion from the gas phase ( $\text{BCl}_3$ ) at  $985 \text{ } ^\circ\text{C}$  on the rear surface. Layers of  $\text{SiO}_2$  and  $\text{Si}_3\text{N}_4$  were formed on the front surface of the SC to passivate the surface and reduce the optical reflectance. The solid and grid aluminum contacts were formed by magnetron sputtering on the rear and front surfaces, respectively. The schematic structure of SC is presented in Fig. 1.

In the case of USL, the transverse or longitudinal AWs were applied to the samples in [100] direction by using  $\text{LiNbO}_3$  or ceramic piezoelectric transducer. The transducer was attached to the whole area of Al back contact. It is widely known that the efficiency of ultrasound influence on defects in semiconductors depends on acoustic wave frequency  $f_{\text{US}}$ . Moreover, the type of frequency dependence is determined by the mechanism of acousto-defect interaction [23–25]. The set of frequencies (2.4, 4.1, 5.4, 9.0, 14, 18, and 31 MHz, longitudinal waves) was used to establish features of ultrasound influence on iron migration. Besides, the effect of the increase in the carrier capture coefficient for defects in silicon SC is shown [26] to be intensified in the case of the transverse acoustic waves using. Accordingly, the transverse waves ( $f_{\text{US}} = 0.3 \text{ MHz}$ ) were used as well. The ultrasound intensities  $W_{\text{US}}$  did not overcome  $1.3 \text{ W/cm}^2$ . To avoid the effect of the piezoelectric field on the measurements procedure as well as sample

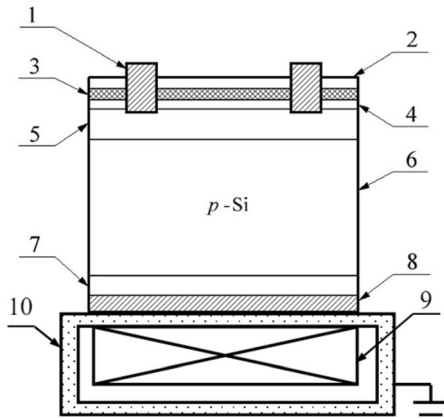


**Fig. 1** Schematic structure of the sample and USL. 1—frontal grid electrode (Al); 2— $\text{Si}_3\text{N}_4$  (40 nm); 3— $\text{SiO}_2$  (30 nm); 4—induced  $n^{++}$ -layer; 5—diffusion  $n^+$ -layer; 6—quasineutral base region of  $p$ -type (350  $\mu\text{m}$ ); 7—diffusion  $p^+$ -layer; 8—rear metallization (Al); 9—piezoelectric transducer; 10—metal foil (Cu)

parameters, the transducer was shielded by Cu foil—see Fig. 1.

It is known that Fe in silicon can be in two states: in the form of FeB pair or in the interstitial state  $\text{Fe}_i$ . At near room temperature and boron concentration  $> 10^{14} \text{ cm}^{-3}$ , almost all Fe bound in FeB pairs is in equilibrium [27–30]. However, numerous researches show that dissociation of pairs can be performed either by heating to the temperature above 200 °C or by intense illumination at room temperature [28, 30]. In our work, we used the latter approach, and the high-intensive illumination source was a halogen lamp with a radiation intensity of about 250 mW/cm<sup>2</sup>. To dissociate FeB pairs, the front side of the sample was illuminated, and the illumination time was 30 s.

The different light-induced degradation (LID) phenomena exist that affect the efficiency of Cz-silicon solar cells due to a decrease in the lifetime of generated excess charge carriers. The main reasons for this transformation are boron-oxygen complex formation (BO-LID) [31] and iron-boron pair dissociation. Besides, the light- and elevated-temperature-induced degradation (LeTID) is observed. In recent studies, the occurrence of the LeTID defect is related to the presence of hydrogen and metal impurities [32–34]. The complete recovery in the dark at near room temperature and the determined value of activation energy (0.656 eV, see below) evidenced the iron-boron pair-related LID in our case.

It is known that FeB pair dissociations in the SC base are accompanied by the change in the lifetime of minority carriers  $\tau$ . As an indicator of  $\tau$ , we considered short circuit current  $I_{\text{SC}}$ , which was measured under SC illumination by a low-intensive monochromatic light. The low-intensive source was a light-emitting diode (LED) with radiation power  $P_{\text{ph}}$  350  $\mu\text{W}$  (measured by PowerMeter Rk-5720) and wavelength  $\lambda = 940 \text{ nm}$ .

The kinetics of short circuit current was measured after high-intensive illumination (see Fig. 2). The measurements were carried out over a temperature range of 300–340 K. The temperature was varied by a thermoelectric cooler and stabilized by a computer-controlled PID loop to better than 0.05 K. The temperature was controlled by STS-21 sensor, which was placed on the front surface of SC.

The FeB pair association in the dark was accompanied by the  $\tau$  increase and was monitored by measuring the  $I_{\text{SC}}$  under LED illumination with 940 nm wavelength. The LED illumination induced excess carrier density  $\Delta n < 10^{12} \text{ cm}^{-3}$ , had duty cycle 0.5% while  $I_{\text{SC}}(t)$  measuring, and did not cause FeB dissociation. Moreover, the fitting of the measured dependencies  $I_{\text{SC}}(t)$  after high-intensive illumination allows determining the pair concentration and the characteristic time of the FeB complex formation. In fact, in conditions of homogeneous carrier generation in the base by the LED illumination, the short circuit current can be described as follows [35, 36]:

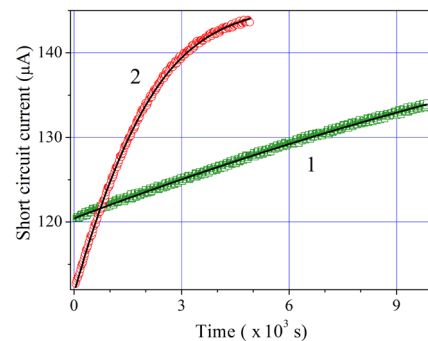


**Fig. 2** Measured under low-intensive (LED) illumination short circuit current plotted as a function of the time after high-intensive (halogen lamp) illumination. The marks are the experimental results, the lines are the fitted curves using Eqs. (1)–(9). The zero of time corresponds to the moment of intensive illumination termination.  $T$ , K: 300 (1, green squares), 330 (2, red circles) (Color figure online)

$$I_{SC}(t) = \frac{P_{ph}(1 - R_{ph})q\beta\lambda}{hc} \frac{\alpha_{ph}L_n(t)}{1 + \alpha_{ph}L_n(t)}, \quad (1)$$

where  $P_{ph}$  is the LED light power,  $\lambda$  is the light wavelength (940 nm),  $q$  is elementary charge,  $h$  is the Planck constant,  $c$  is the speed of light,  $\alpha_{ph} = \alpha_{ph}(T, \lambda)$  is the coefficient of light absorption, which was calculated according to [37, 38],  $T$  is the cell temperature,  $R_{ph}(\lambda)$  is the coefficient of reflection, which was calculated for used samples according to [39, 40],  $R_{ph}(940 \text{ nm}) = 0.14$ ;  $\beta$  is the coefficient of quantum yield,  $\beta = 1$ ;  $L_n$  is the diffusion length of minority carriers. In its turn

$$L_n(t) = \sqrt{\frac{\mu_n k T \tau(t)}{q}}, \quad (2)$$

where  $\mu_n$  is the electron mobility, was calculated by Klaassen theory [41],  $k$  is the Boltzmann constant.

In the assumption that it is the iron-related defects that play an essential role in the recombination, the following expression can be used to estimate  $\tau$  according to Mattisen rule:

$$\tau(t)^{-1} = \tau_{rad}^{-1} + \tau_{Aug}^{-1} + [\tau_{SRH}^{Fe_i}(t)]^{-1} + [\tau_{SRH}^{FeB}(t)]^{-1} + \tau_{other}^{-1}, \quad (3)$$

where  $\tau_{rad}$  and  $\tau_{Aug}$  are associated with band-to-band radiation recombination and Auger processes, respectively;  $\tau_{SRH}^{Fe_i}$  and  $\tau_{SRH}^{FeB}$  are related to the recombinations at interstitial iron atoms  $Fe_i$  and at FeB pairs, accordingly;  $\tau_{other}$  describes further recombination channels including surface recombination. In turn,

$$\tau_{rad}^{-1} = B(N_A + n_0 + \Delta n), \quad (4)$$

$$\tau_{Aug}^{-1} = C_p N_A^2, \quad (5)$$

where the values of recombination coefficients  $B$  and  $C_p$  were calculated by data from [42, 43];  $n_0 = n_i^2/N_A$  and intrinsic carrier concentration  $n_i$  was taken from [44].

In order to calculate  $\tau_{SRH}^{Fe_i}$  and  $\tau_{SRH}^{FeB}$ , Shockley–Read–Hall model was used:

$$\tau_{SRH}^{Fe_i, FeB}(t) = \frac{\tau_{p0}(t)(n_0 + n_1 + \Delta n) + \tau_{n0}(t)(N_A + p_1 + \Delta n)}{N_A + n_0 + \Delta n}, \quad (6)$$

where  $\tau_{p0}(t) = [N_{trap}(t)\sigma_p n v_{th}^{p,n}]^{-1}$ ,  $N_{trap}(t)$  is the trap concentration ( $N_{Fe_i}$  and  $N_{FeB}$  for  $Fe_i$  and FeB,

respectively),  $\sigma_n$ ,  $\sigma_p$  are the cross sections of the recombination centers for electrons and holes, respectively,  $v_{th}^n$ ,  $v_{th}^p$  are the average thermal velocities of electrons and holes calculated according to [45],  $n_1 = N_C \exp[-(E_C - E_t)/kT]$ ,  $p_1 = N_V \exp[-(E_t - E_V)/kT]$ ;  $N_C$  and  $N_V$  are the densities of states in the conduction band and valence band, respectively [44];  $E_C$  and  $E_V$  are the energy of the conduction band and valence band edge, respectively;  $E_t$  is the energy level of the relevant recombination level. The parameters of recombination centers related to  $Fe_i$  and FeB were taken from [46].

The time dependence of interstitial iron atom concentration after pair dissociations is described by the known expression from [47]:

$$N_{Fe_i}(t) = (N_{Fe_i,0} - N_{Fe_i,eq}) \cdot \exp(-t/\tau_{ass}) + N_{Fe_i,eq}, \quad (7)$$

where  $\tau_{ass}$  is the characteristic time of the formation of FeB pair,  $N_{Fe_i,0}$  is the concentration of interstitial iron atoms formed due to high-intensive illumination,  $N_{Fe_i,eq}$  is the part of interstitial iron atoms with  $N_{Fe_i,0}$  that remain unpaired in equilibrium state (after a long exposition in darkness)[27]:

$$N_{Fe_i,eq} = \frac{N_{Fe_i,0}}{\left[1 + N_A 10^{-23} \exp\left(\frac{0.582 \text{ eV}}{kT}\right)\right] \left[1 + \exp\left(-\frac{E_F - 0.394 \text{ eV}}{kT}\right)\right]}, \quad (8)$$

$E_F$  is the quasi Fermi level.

In its turn, the iron–boron pair concentration  $N_{FeB}$ , which formed as the result of the partial association of  $N_{Fe_i,0}$ , should be described by the following expression:

$$N_{FeB}(t) = N_{Fe_i,0} - N_{Fe_i}(t). \quad (9)$$

We used Eqs. (1)–(9) to fit the measured time dependencies of short circuit current—see the examples in Fig. 2. The fitting was performed by using metaheuristic method EBLSHADE [48]; as fitting parameters,  $P_{ph}$ ,  $\tau_{other}$ ,  $N_{Fe_i,0}$ , and  $\tau_{ass}$  were taken. Thus, for the experimental data given in Fig. 2, the following parameter values were determined.  $P_{ph} = (3.2 \pm 0.3) \times 10^{-4} \text{ W}$ , which agrees well with the measured by PowerMeter Rk-5720 value (350  $\mu\text{W}$ ).  $\tau_{other} > 100 \text{ s}$ , which testifies that the other recombination channel (other impurities, lattice defects, surface recombination) can be neglected.



$N_{\text{Fe},0} = (7 \pm 1) \times 10^{12} \text{ cm}^{-3}$ , which is, on the one hand, a typical value for solar silicon, and, on the other hand, it is close to  $3 \times 10^{12} \text{ cm}^{-3}$  obtained for the samples of the same series from  $L_n$  measuring before and after high-intense illumination [49]. Finally, the values of  $\tau_{\text{ass}}$  were found to be  $(1380 \pm 20) \text{ s}$  at  $T = 330 \text{ K}$  and  $(1.26 \pm 0.02) \times 10^4 \text{ s}$  at  $T = 300 \text{ K}$ . It was reported that  $\tau_{\text{ass}}$  depends on the boron concentration and temperature, and the following expression was proposed for association characteristic time [28]:

$$\tau_{\text{ass}} = \frac{5.7 \times 10^5 T}{N_A} \exp\left(\frac{E_m}{kT}\right), \quad (10)$$

where  $E_m$  is the energy of  $\text{Fe}_i$  migration.

The value  $E_m = (0.656 \pm 0.002) \text{ eV}$  was calculated by using Eq. (10) and  $\tau_{\text{ass}}$ , which determined from experiment. This value coincides with the well-known [28, 50] value of  $0.66 \text{ eV}$ . The coincidence proves that the measuring of the time dependence of short circuit current after high-intense illumination can be applied in finding such parameters of iron-related defects as FeB pair association time and Fe concentration.

### 3 Results and discussion

The typical dependencies  $I_{\text{SC}}(t)$ , measured at different temperatures under USL conditions and without USL, are given in Fig. 3. The experiments have shown that the US loading leads to a speed-up of recovery of short circuit current after high-intense illumination. Therefore, the FeB association is intensified under AW action. The pair formation time constant, determined by the measured data fitting in the case of ultrasound loading, will be referred to as  $\tau_{\text{US}}$  ( $\tau_{\text{US}} = \tau_{\text{ass}}@W_{\text{US}} > 0$ ). In its turn, the time constant, determined in the case without ultrasound, will be referred to as  $\tau_0$  ( $\tau_0 = \tau_{\text{ass}}@W_{\text{US}} = 0$ ).  $\tau_{\text{US}}$  and  $\tau_0$  are given in Fig. 3 as well. As seen,  $\tau_{\text{US}}/\tau_0 < 1$ . To evaluate the acoustically induced accelerating of FeB pair formation, the  $\tau_{\text{US}}/\tau_0$  magnitude will be used hereafter.

The obtained results show that the magnitude of speed-up of FeB pair formation depends on AW intensity. As shown in Fig. 4, the  $\tau_{\text{US}}$  decreases with the increase in ultrasound intensity, and the dependence of  $\tau_{\text{US}}$  on  $W_{\text{US}}$  is close to linear at low values

of intensity. The increase in  $W_{\text{US}}$  leads to the  $\tau_{\text{US}}$  saturation. In the saturation case,  $\tau_{\text{US}}$  equals to about  $0.7\tau_0$  at  $340 \text{ K}$ .

Also, Fig. 4 shows that the efficiency of AI accelerating of FeB pair formation decreases with the increase in US frequency. This feature is observed for the samples with different iron content. The iron concentrations were determined by fitting of  $I_{\text{SC}}(t)$  dependencies, which were measured at complete FeB pairs dissociation conditions (i.e., in the case of high-intense illumination with duration  $\geq 30 \text{ s}$ , which cause a maximum decrease in short circuit current value). The US intensity  $W_{\text{US,sat}}$ , which corresponds to saturation in  $\tau_{\text{US}}/\tau_0$ , depends on  $f_{\text{US}}$  as well: in fact,  $W_{\text{US,sat}} \simeq 0.6 \text{ W/cm}^2$  at  $f_{\text{US}} = 2.4 \text{ MHz}$  and  $W_{\text{US,sat}} \simeq 0.9 \text{ W/cm}^2$  at  $f_{\text{US}} = 9.0 \text{ MHz}$ —see Fig. 4b. At the same time, the saturation magnitude of  $\tau_{\text{US}}/\tau_0$  does not depend on  $f_{\text{US}}$ . Transverse waves, despite lower frequency, affect the processes of FeB pair formation more weakly. It is previously shown [26] that the acoustically induced change of complex defect parameters can be attributed to the variation in the distance of the components, and this effect is intensified in the case of the transverse waves. The opposite feature of investigated phenomenon testifies that the AI acceleration of the FeB pair association does not deal with change in the iron–boron distance. The following figure, Fig. 5, presents  $\tau_{\text{US}}/\tau_0$  dependencies for the samples with different iron concentrations under USL of the same US frequency. As seen from the figure, the AI effect does not practically depend on  $N_{\text{Fe},0}$ .

Figure 6 illustrates the variation of US impact on the characteristic FeB pair association time over the explored temperature range. The data for  $f_{\text{US}} = 9.0 \text{ MHz}$  is correspond to the saturation region of  $\tau_{\text{US}}/\tau_0 = f(W_{\text{US}})$  dependency, other data—to the linear region. As seen from the figure, the temperature decrease causes the decrease in efficiency of US influence, and the dependencies of  $\tau_{\text{US}}/\tau_0$  on  $T$  are close to linear.

The association of the FeB complex happens at the expense of  $\text{Fe}_i$  diffusion toward the boron atoms located in substituting positions and strongly bound with the neighbor due to forming covalent bonds with them. Therefore, the  $\tau_{\text{ass}}$  depends on the coefficient of iron diffusion  $D_{\text{Fe}}$ , so a more detailed, in

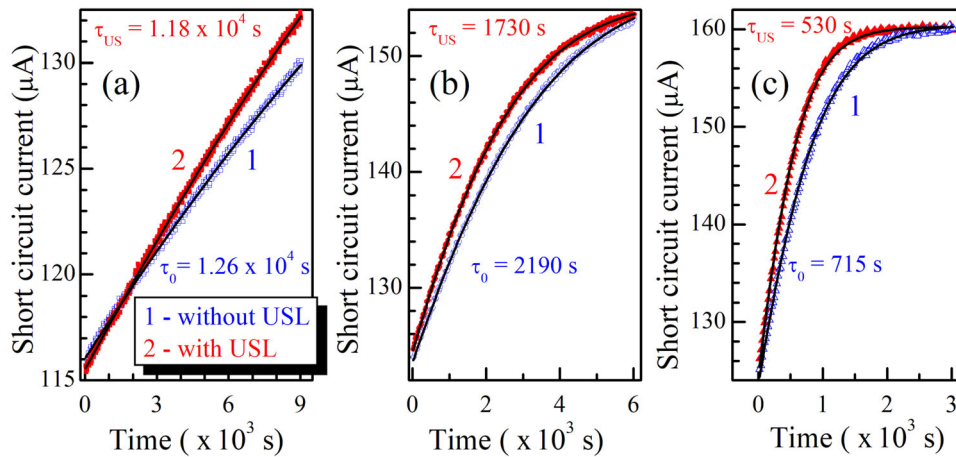


**Fig. 3** Measured short circuit current plotted as a function of the time after high-intensive illumination under USL (2, filled red marks,  $f_{US} = 2.4$  MHz) and without USL (1, empty blue marks). The lines are the fitted curves using Eqs. (1)–(9).  $T$ , K: 300 (a),

320 (b), 340 (c). The pair formation time constants determined by the fitting are shown as well;  $\tau_{US}$  (red)—with USL and  $\tau_0$  (blue)—without USL (Color figure online)

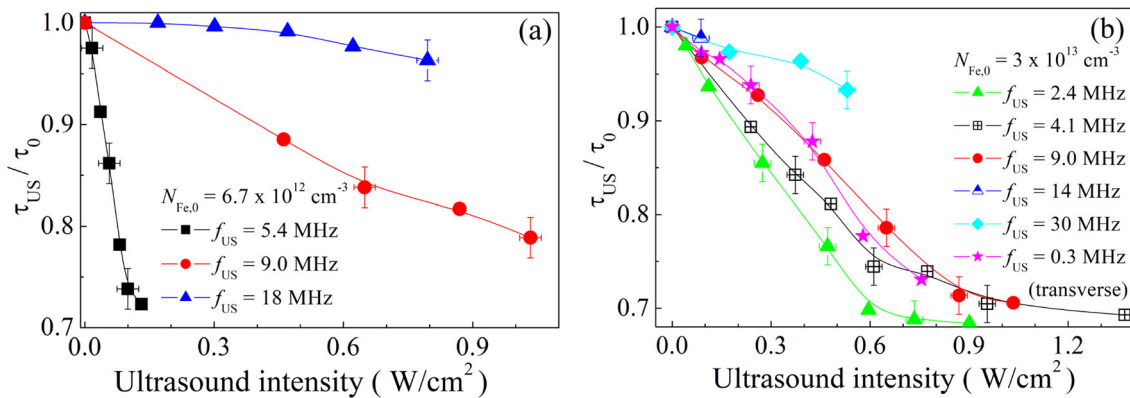


**Fig. 4** Dependencies of AI accelerating of FeB pair formation on the US intensity at different  $f_{US}$ . Parts **a** and **b** present results for the Si solar cells with different iron concentrations.  $T = 340$  K. The marks are the experimental results, the lines are given for convenience only

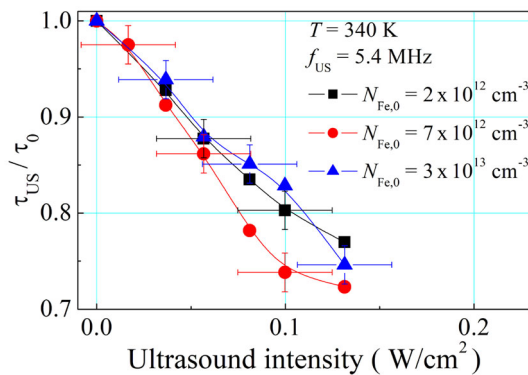


**Fig. 5** Dependencies of AI accelerating of FeB pair formation on the US intensity in solar cells with different iron content.  $T = 340$  K.  $f_{US} = 5.4$  MHz. The marks are the experimental results, the lines are given for convenience only

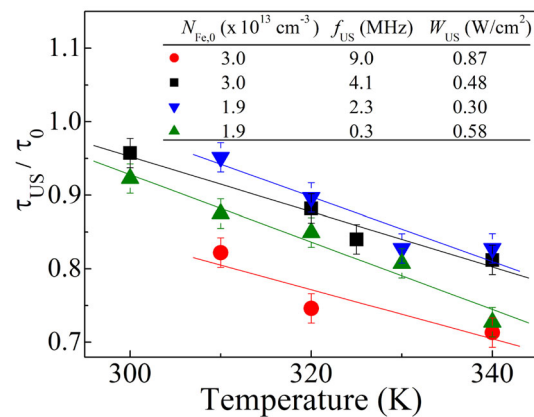


**Fig. 6** Temperature dependencies of AI accelerating of FeB pair formation. The marks are the experimental results, the lines are the linear fitted curves

comparison with Eq. (10), the expression takes the following form [28, 30, 51]:

$$\tau_{\text{ass}} = \frac{\varepsilon \varepsilon_0 kT}{q^2 D_{\text{Fe}} N_A} = \frac{\varepsilon \varepsilon_0 kT}{q^2 D_{0,\text{Fe}} N_A} \exp\left(\frac{E_m}{kT}\right), \quad (11)$$

where  $\varepsilon$  is the dielectric constant of silicon,  $\varepsilon_0$  is the vacuum permittivity,  $D_{\text{Fe}} = D_{0,\text{Fe}} \exp(-E_m/kT)$ ,  $D_{0,\text{Fe}}$  is the temperature-independent multiplier, in the general case [52–54]  $D_{0,\text{Fe}} = \beta v a^2 \exp(\delta S_{\text{Fe}}/k)$ ,  $\beta$  is the correlation factor,  $v$  is the effective vibrational (attempt) frequency,  $a$  is the jump distance,  $\delta S_{\text{Fe}}$  is the migration entropy.

As seen from the Eq. (11), the decrease FeB pair formation time under USL condition testifies about AI increase in  $D_{\text{Fe}}$ . In our opinion, the most probable reason is AI decrease in iron migration energy—see Fig. 7. Enhanced diffusion of impurities in the US field was observed previously in poly- and single-crystals of silicon and gallium arsenide [55, 56]. The decrease in interstitial iron atom migration energy can be given as

$$E_m \xrightarrow{\text{ultrasound}} E_{m,0} - \Delta E_{\text{US}} \quad (12)$$

where  $E_{m,0}$  is the migration energy without USL, according to [28, 50] and our estimation,  $E_{m,0} \sim 0.66$  eV;  $\Delta E_{\text{US}}$  is the AI change in migration energy. According to the obtained results, energy change depends on temperature and US characteristics ( $\Delta E_{\text{US}} = f(W_{\text{US}}, f_{\text{US}}, \text{wave type}, T)$ ) and does not exceed 10 meV.

The mechanism of the found AI phenomenon can be the following. By using thermodynamic formalism, it was shown [52] that the ability of impurities in Si to diffuse depends on mechanical stress  $\eta$ :

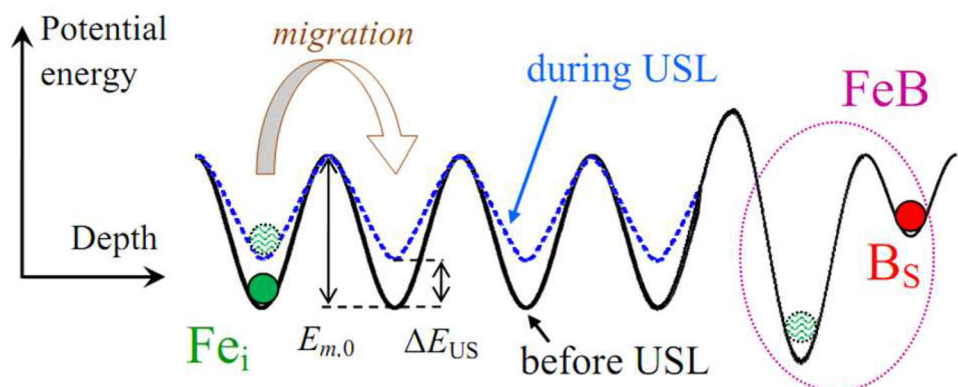
$$\frac{D(\eta)}{D(0)} = \exp\left(\frac{\eta V^*}{kT}\right) = \exp\left(\frac{\eta[-\Omega + V^r + V^m]}{kT}\right), \quad (13)$$

where  $V^*$  is the activation strain tensor,  $\Omega$  is the atomic volume representing crystal dimension changes upon the formation of lattice site before the lattice relaxation around the newly created point defect is permitted,  $V^r$  is the relaxation volume,  $V^m$  is the migration strain tensor, which characterizes stress impact on the defect mobility. The enhance Fe<sub>i</sub> diffusivity in the strain field is discussed in [57] as well.

In our opinion, this reason explains the found US impact on FeB pairs formation in silicon solar cell. In fact, as seen from the Eq. (13), the stress-induced change in diffusion coefficient is thermally activated. As a result, the AI variation in  $\tau_{\text{ass}}$  depends on temperature. In addition, generally  $V^*$  contains 81 components [52]; therefore change in  $D_{\text{Fe}}$  depends on the direction of atom elastic displacements. This accounts for the less effective impact of transverse waves. It should be noted that, the absorption of oscillation energy is used [58, 59] to reveal the cause of USL impact on defect system in Si–SiO<sub>2</sub> structures, and, in particular, AI increase in impurities mobility.

The results reported here open up new possibilities in manipulating electronic properties of silicon barrier devices. For example, as mentioned above, during phosphor diffusion, the iron impurity gettering occurs as well. The diffusion happens at high temperatures, and iron is in an unpaired interstitial state. USL applied during this technological process should increase the degree of the SC base region cleaning due to AI increase in Fe diffusion coefficient and, as a result, improve SC performance.

**Fig. 7** A schematic picture showing the spatial variation of the potential energy of iron interstitial atom in Si as a function of position near the boron substitutional atom. US stress lowers the energy barrier for Fe migration. The curves are scaled arbitrarily



## 4 Conclusion

The ultrasound influence on Fe<sub>2</sub>B pair formation in silicon solar cells has been investigated experimentally. The investigation has revealed an acoustically driven decrease in the association characteristic time, which was caused by enhancing in iron atom diffusivity under ultrasound action. The effect is intensified with the increase in temperature and the decrease in ultrasound frequency. The application of longitudinal acoustic waves is more effective than transverse waves. The phenomenon can be related to reducing iron migration energy (up to 10 meV) in silicon under ultrasound stress at nearly-room temperature. Thus, ultrasound can be an effective functional tool for controlling silicon structure characteristics.

## Author contributions

All authors contributed equally to this work.

## Funding

This work was supported by National Research Foundation of Ukraine (Project Number 2020.02/0036).

## Data availability

Some or all data generated or used during the study are available from the corresponding author by request.

## Declarations

**Conflict of interest** There are no conflict to declare.

## References

1. S.S. Ostapenko, N.E. Korsunskaya, M.K. Sheinkman, Ultrasound stimulated defect reactions in semiconductors, in *Defect Interaction and Clustering in Semiconductors. Solid State Phenomena*, vol. 85–86, (Trans Tech Publications, Zürich, 2002), pp. 317–336. <https://doi.org/10.4028/www.scientific.net/SSP.85-86.317>
2. R.K. Savkina, Recent progress in semiconductor properties engineering by ultrasonication. *Recent Patents Electr. Electron. Eng.* **6**(3), 157–172 (2013). <https://doi.org/10.2174/22131116113066660008>
3. O.Y. Olikh, A.M. Gorb, R.G. Chupryna, O.V. Pristay-Fenenkov, Acousto-defect interaction in irradiated and non-irradiated silicon  $n^+p$  structure. *J. Appl. Phys.* **123**(16), 161573 (2018). <https://doi.org/10.1063/1.5001123>
4. A. Davletova, S.Z. Karazhanov, Open-circuit voltage decay transient in dislocation-engineered Si p–n junction. *J. Phys. D Appl. Phys.* **41**(16), 165107 (2008). <https://doi.org/10.1088/0022-3727/41/16/165107>
5. Y. Olikh, M. Tymochko, O. Olikh, Mechanisms of two-stage conductivity relaxation in CdTe:Cl with ultrasound. *J. Electron. Mater.* **49**(8), 4524–4530 (2020). <https://doi.org/10.1007/s11664-020-08179-7>
6. O. Olikh, Reversible influence of ultrasound on  $\gamma$ -irradiated Mo/n-Si Schottky barrier structure. *Ultrasonics* **56**, 545–550 (2015). <https://doi.org/10.1016/j.ultras.2014.10.008>
7. O.Y. Olikh, K.V. Voytenko, R.M. Burbelo, Ultrasound influence on I–V–T characteristics of silicon Schottky barrier structure. *J. Appl. Phys.* **117**(4), 044505 (2015). <https://doi.org/10.1063/1.4906844>
8. A.V. Sukach, V.V. Teterkin, Ultrasonic treatment-induced modification of the electrical properties of InAs p–n junctions. *Tech. Phys. Lett.* **35**(6), 514–517 (2009). <https://doi.org/10.1134/S1063785009060108>
9. D. Krüger, B. Romanyuk, V. Melnik, Y. Olikh, R. Kurps, Influence of in situ ultrasound treatment during ion implantation on amorphization and junction formation in silicon. *J. Vac. Sci. Technol. B* **20**(4), 1448–1451 (2002). <https://doi.org/10.1116/1.1493784>
10. B. Romanyuk, V. Melnik, Y. Olikh, V. Popov, D. Krüger, Modification of the Si amorphization process by in situ ultrasonic treatment during ion implantation. *Semicond. Sci. Technol.* **16**(5), 397–401 (2001). <https://doi.org/10.1088/0268-1242/16/5/320>
11. S. Kalem, O. Yavuzcetin, C. Altineller, Effect of light exposure and ultrasound on the formation of porous silicon. *J. Porous Mater.* **7**(1), 381–383 (2000). <https://doi.org/10.1023/A:1009687021287>
12. S. Fujita, K. Kaneko, T. Ikenoue, T. Kawaharamura, M. Furuta, Ultrasonic-assisted mist chemical vapor deposition of II-oxide and related oxide compounds. *Phys. Status Solidi C* **11**(7–8), 1225–1228 (2014). <https://doi.org/10.1002/pssc.201300655>
13. A.A. Istratov, H. Hieslmair, E.R. Weber, Iron and its complexes in silicon. *Appl. Phys. A Mater. Sci. Process.* **69**(1), 13–44 (1999). <https://doi.org/10.1007/s003390050968>



14. M.C. Schubert, M. Padilla, B. Michl, L. Mundt, J. Giesecke, J. Hohl-Ebinger, J. Benick, W. Warta, M. Tajima, A. Ogura, Iron related solar cell instability: Imaging analysis and impact on cell performance. *Sol. Energy Mater. Sol. Cells* **138**, 96–101 (2015). <https://doi.org/10.1016/j.solmat.2015.03.001>
15. H.S. Laine, V. Vähänissi, A.E. Morishige, J. Hofstetter, A. Haarahiltunen, B. Lai, H. Savin, D.P. Fenning, Impact of iron precipitation on phosphorus-implanted silicon solar cells. *IEEE J. Photovolt.* **6**(5), 1094–1102 (2016). <https://doi.org/10.1109/JPHOTOV.2016.2576680>
16. V. Vähänissi, A. Haarahiltunen, H. Talvitie, M. Yli-Koski, H. Savin, Impact of phosphorus gettering parameters and initial iron level on silicon solar cell properties. *Prog. Photovolt. Res. Appl.* **21**(5), 1127–1135 (2013). <https://doi.org/10.1002/pip.2215>
17. T. Mchedlidze, C. Möller, K. Lauer, J. Weber, Evolution of iron-containing defects during processing of Si solar cells. *J. Appl. Phys.* **116**(24), 245701 (2014). <https://doi.org/10.1063/1.4905027>
18. T. Bartel, F. Gibaja, O. Graf, D. Gross, M. Kaes, M. Heuer, F. Kirscht, C. Möller, K. Lauer, Dynamics of iron-acceptor-pair formation in co-doped silicon. *Appl. Phys. Lett.* **103**(20), 202109 (2013). <https://doi.org/10.1063/1.4830227>
19. J. Ajayan, D. Nirmal, P. Mohankumar, M. Saravanan, M. Jagadesh, L. Arivazhagan, A review of photovoltaic performance of organic/inorganic solar cells for future renewable and sustainable energy technologies. *Superlattices Microstruct.* **143**, 106549 (2020). <https://doi.org/10.1016/j.spmi.2020.106549>
20. M.A. Green, Photovoltaic technology and visions for the future. *Prog. Energy* **1**(1), 013001 (2019). <https://doi.org/10.1088/2516-1083/ab0fa8>
21. S.S. Ostapenko, L. Jastrzebski, J. Lagowski, B. Sopori, Increasing short minority carrier diffusion lengths in solar-grade polycrystalline silicon by ultrasound treatment. *Appl. Phys. Lett.* **65**(12), 1555–1557 (1994). <https://doi.org/10.1063/1.112942>
22. S.S. Ostapenko, R.E. Bell, Ultrasound stimulated dissociation of Fe–B pairs in silicon. *J. Appl. Phys.* **77**(10), 5458–5460 (1995). <https://doi.org/10.1063/1.359243>
23. A.D. Brailsford, Abrupt-kink model of dislocation motion. *Phys. Rev.* **122**(3), 778–786 (1961). <https://doi.org/10.1103/PhysRev.122.778>
24. V.N. Pavlovich, Enhanced diffusion of impurities and defects in crystals in conditions of ultrasonic and radiative excitation of the crystal lattice. *Phys. Status Solidi B* **180**(1), 97–105 (1993). <https://doi.org/10.1002/pssb.2221800108>
25. R.M. Peleshchak, O.V. Kuzyk, O.O. Dan'kiv, Formation of periodic structures under the influence of an acoustic wave in semiconductors with a two-component defect subsystem. *Ukr. J. Phys.* **61**(8), 741–746 (2016). <https://doi.org/10.15407/ujpe.61.08.0741>
26. O.Y. Olikh, Acoustically driven degradation in single crystalline silicon solar cell. *Superlattices Microstruct.* **117**, 173–188 (2018). <https://doi.org/10.1016/j.spmi.2018.03.027>
27. W. Wijaranakula, The reaction kinetics of iron–boron pair formation and dissociation in p-type silicon. *J. Electrochem. Soc.* **140**(1), 275–281 (1993). <https://doi.org/10.1149/1.2056102>
28. C. Möller, T. Bartel, F. Gibaja, K. Lauer, Iron–boron pairing kinetics in illuminated p-type and in boron/phosphorus co-doped n-type silicon. *J. Appl. Phys.* **116**(2), 024503 (2014). <https://doi.org/10.1063/1.4889817>
29. J. Tan, D. Macdonald, F. Rougieux, A. Cuevas, Accurate measurement of the formation rate of iron–boron pairs in silicon. *Semicond. Sci. Technol.* **26**(5), 055019 (2011). <https://doi.org/10.1088/0268-1242/26/5/055019>
30. D. Macdonald, T. Roth, P.N.K. Deenapanray, K. Bothe, P. Pohl, J. Schmidt, Formation rates of iron-acceptor pairs in crystalline silicon. *J. Appl. Phys.* **98**(8), 083509 (2005). <https://doi.org/10.1063/1.2102071>
31. J. Lindroos, H. Savin, Review of light-induced degradation in crystalline silicon solar cells. *Sol. Energy Mater. Sol. Cells* **147**, 115–126 (2016). <https://doi.org/10.1016/j.solmat.2015.11.047>
32. A. Schmid, C. Fischer, D. Skorka, A. Herguth, C. Winter, A. Zuschlag, G. Hahn, On the role of AlO<sub>x</sub> thickness in AlO<sub>x</sub>/SiN<sub>y</sub>: H layer stacks regarding light- and elevated temperature-induced degradation and hydrogen diffusion in c-Si. *IEEE J. Photovolt.* **11**(4), 967–973 (2021). <https://doi.org/10.1109/JPHOTOV.2021.3075850>
33. M. Wagner, F. Wolny, M. Hentsche, A. Krause, L. Sylla, F. Kropfgans, M. Ernst, R. Zierer, P. Bönisch, P. Müller, N. Schmidt, V. Osinniy, H.-P. Hartmann, R. Mehnert, H. Neuhaus, Correlation of the LeTID amplitude to the Aluminium bulk concentration and Oxygen precipitation in PERC solar cells. *Sol. Energy Mater. Sol. Cells* **187**, 176–188 (2018). <https://doi.org/10.1016/j.solmat.2018.06.009>
34. D. Chen, M. Kim, B.V. Stefani, B.J. Hallam, M.D. Abbott, C.E. Chan, R. Chen, D.N.R. Payne, N. Nampalli, A. Ciesla, T.H. Fung, K. Kim, S.R. Wenham, Evidence of an identical firing-activated carrier-induced defect in monocrystalline and multicrystalline silicon. *Sol. Energy Mater. Sol. Cells* **172**, 293–300 (2017). <https://doi.org/10.1016/j.solmat.2017.08.003>
35. A. Fahrenbruch, R. Bube, *Fundamentals of Solar Cells: Photovoltaic Solar Energy Conversion* (Academic Press, London, Paris, 1983), p. 580

36. M. Razeghi, A. Rogalski, Semiconductor ultraviolet detectors. *J. Appl. Phys.* **79**(10), 7433–7473 (1996). <https://doi.org/10.1063/1.362677>
37. K. Rajkanan, R. Singh, J. Shewchun, Absorption coefficient of silicon for solar cell calculations. *Solid-State Electron.* **22**(9), 793–795 (1979). [https://doi.org/10.1016/0038-1101\(79\)90128-X](https://doi.org/10.1016/0038-1101(79)90128-X)
38. M.A. Green, M.J. Keevers, Optical properties of intrinsic silicon at 300 K. *Progr. Photovolt. Res. Appl.* **3**(3), 189–192 (1995). <https://doi.org/10.1002/pip.4670030303>
39. N.I. Klyui, V.P. Kostilyov, A.G. Rozhin, V.I. Gorbulyk, V.G. Litovchenko, M.A. Voronkin, N.I. Zaika, Silicon solar cells with antireflecting and protective coatings based on diamond-like carbon and silicon carbide films. *Opto-Electr. Rev.* **8**(4), 402–405 (2000)
40. V.G. Litovchenko, N.I. Klyui, V.P. Kostilyov, V.I. Gorbulyk, Y.P. Piryatinskii, Nitrogen containing diamond-like carbon films as protective and fluorescent layers for silicon solar cells. *Opto-Electr. Rev.* **8**(4), 406–409 (2000)
41. D.B.M. Klaassen, A unified mobility model for device simulation—I. Model equations and concentration dependence. *Solid-State Electron.* **35**(7), 953–959 (1992). [https://doi.org/10.1016/0038-1101\(92\)90325-7](https://doi.org/10.1016/0038-1101(92)90325-7)
42. H.T. Nguyen, S.C. Baker-Finch, D. Macdonald, Temperature dependence of the radiative recombination coefficient in crystalline silicon from spectral photoluminescence. *Appl. Phys. Lett.* **104**(11), 112105 (2014). <https://doi.org/10.1063/1.4869295>
43. P.P. Altermatt, J. Schmidt, G. Heiser, A.G. Aberle, Assessment and parameterisation of Coulomb-enhanced Auger recombination coefficients in lowly injected crystalline silicon. *J. Appl. Phys.* **82**(10), 4938–4944 (1997). <https://doi.org/10.1063/1.366360>
44. R. Couderc, M. Amara, M. Lemiti, Reassessment of the intrinsic carrier density temperature dependence in crystalline silicon. *J. Appl. Phys.* **115**(9), 093705 (2014). <https://doi.org/10.1063/1.4867776>
45. M.A. Green, Intrinsic concentration, effective densities of states, and effective mass in silicon. *J. Appl. Phys.* **67**(6), 2944–2954 (1990). <https://doi.org/10.1063/1.345414>
46. F.E. Rougieux, C. Sun, D. Macdonald, Determining the charge states and capture mechanisms of defects in silicon through accurate recombination analyses: a review. *Sol. Energy Mater. Sol. Cells* **187**, 263–272 (2018). <https://doi.org/10.1016/j.solmat.2018.07.029>
47. J.D. Murphy, K. Bothe, M. Olmo, V.V. Voronkov, R.J. Falster, The effect of oxide precipitates on minority carrier lifetime in p-type silicon. *J. Appl. Phys.* **110**(5), 053713 (2011). <https://doi.org/10.1063/1.3632067>
48. A.W. Mohamed, A.A. Hadi, K.M. Jambi, Novel mutation strategy for enhancing SHADE and LSHADE algorithms for global numerical optimization. *Swarm Evol. Comput.* **50**, 100455 (2019). <https://doi.org/10.1016/j.swevo.2018.10.006>
49. G. Zoth, W. Bergholz, A fast, preparation-free method to detect iron in silicon. *J. Appl. Phys.* **67**(11), 6764–6771 (1990). <https://doi.org/10.1063/1.345063>
50. D. Macdonald, A. Cuevas, L.J. Geerligs, Measuring dopant concentrations in compensated p-type crystalline silicon via iron-acceptor pairing. *Appl. Phys. Lett.* **92**(20), 202119 (2008). <https://doi.org/10.1063/1.2936840>
51. N. Khelifati, H.S. Laine, V. Vähänissi, H. Savin, F.Z. Bouamama, D. Bouhafs, Dissociation and formation kinetics of iron–boron pairs in silicon after phosphorus implantation gettering. *Phys. Status Solidi A* **216**(17), 1900253 (2019). <https://doi.org/10.1002/pssa.201900253>
52. M.J. Aziz, Stress effects on defects and dopant diffusion in Si. *Mater. Sci. Semicond. Process.* **4**(5), 397–403 (2001). [https://doi.org/10.1016/S1369-8001\(01\)00014-2](https://doi.org/10.1016/S1369-8001(01)00014-2)
53. M. Stavola (ed.), *Identification of Defects in Semiconductors* (Academic Press, San Diego, 1998)
54. E.R. Weber, Transition metals in silicon. *Appl. Phys. A* **30**(1), 1–22 (1983). <https://doi.org/10.1007/BF00617708>
55. S. Ostapenko, Defect passivation using ultrasound treatment: fundamentals and application. *Appl. Phys. A Mater. Sci. Process.* **69**(2), 225–232 (1999). <https://doi.org/10.1007/s003390050994>
56. B.N. Zaveryukhin, N.N. Zaveryukhina, O.M. Tursunkulov, Variation of the reflection coefficient of semiconductors in a wavelength range from 0.2 to 20  $\mu\text{m}$  under the action of ultrasonic waves. *Tech. Phys. Lett.* **28**(9), 752–756 (2002). <https://doi.org/10.1134/1.1511774>
57. B. Ziebarth, M. Mrovec, C. Elsässer, P. Gumbsch, Influence of dislocation strain fields on the diffusion of interstitial iron impurities in silicon. *Phys. Rev. B* **92**, 115309 (2015). <https://doi.org/10.1103/PhysRevB.92.115309>
58. A.M. Gorb, O.A. Korotchenkov, O.Y. Olikh, A.O. Podolian, R.G. Chupryna, Influence of  $\gamma$ -irradiation and ultrasound treatment on current mechanism in Au–SiO<sub>2</sub>–Si structure. *Solid-State Electron.* **165**, 107712 (2020). <https://doi.org/10.1016/j.sse.2019.107712>
59. D. Kropman, V. Seeman, S. Dolgov, A. Medvids, Effect of ultrasonic treatment on the defect structure of the Si–SiO<sub>2</sub> system. *Phys. Status Solidi C* **13**(10–12), 793–797 (2016). <https://doi.org/10.1002/pssc.201600052>

**Publisher's Note** Springer Nature remains neutral with regard to jurisdictional claims in published maps and institutional affiliations.